# Neutron transition densities from $^{88}Sr(p,p')$ at $E_p = 200$ MeV

J. J. Kelly
*Department of Physics, University of Maryland, College Park, Maryland 20742*

B. S. Flanders
*Department of Physics, American University, Washington, D.C. 20016*

F. W. Hersman, J. H. Heisenberg, J. Calarco, J. P. Connelly,*
and T. E. Milliman
*Department of Physics, University of New Hampshire, Durham, New Hampshire 03824*

A. Scott, F. T. Baker, and V. Penumetcha†
*Department of Physics, University of Georgia, Athens, Georgia 30601*

W. P. Jones, G. T. Emery,‡ A. D. Bacher, and C. Olmer
*Department of Physics, Indiana University, Bloomington, Indiana 47405*

M. A. Grimm
*Department of Physics, University of Louisville, Louisville, Kentucky 40292*

M. L. Whiten
*Department of Physics, Armstrong State College, Savannah, Georgia 31406*
(Received 7 December 1992)

New cross section and analyzing power data for $^{88}Sr(p,p')$ at $E_p = 200$ MeV are reported and analyzed together with earlier cross section data. Neutron transition densities for low-lying normal-parity excitations were extracted using an empirical density-dependent effective interaction and an expansion of the radial density which permits analysis of uncertainties due to penetrability, distortion, incompleteness, statistics, and normalization. The densities were compared with shell-model calculations using effective operators based upon a density-dependent Hartree-Fock approximation. Good agreement between theory and experiment is obtained for the $2_1^+$, $3_1^-$, and $5_1^-$ states, but the experimental neutron densities for the $2_2^+$ and $7_1^-$ states are considerably stronger than expected. Both proton and neutron transition densities for the $2_2^+$ state have strong interior lobes, but the theory fails to reproduce the accompanying surface lobes.

PACS number(s): 25.40.Ep, 27.50.+e, 21.60.Cs

## I. INTRODUCTION

The structure of nuclei near the $N = 50$ shell closure has been investigated with numerous reactions and theoretical techniques [1–10]. The simplest description of $^{88}Sr$ posits two proton holes in the $2p_{1/2}$ orbit, so that low-lying states are largely composed of $\pi(2p_{1/2}, 1f_{5/2}^{-1})$ and $\pi(2p_{1/2}, 2p_{3/2}^{-1})$ configurations. Schwentker *et al.* [1] have shown that appropriate linear combinations of these two configurations provide a good qualitative description of transition charge densities for the two lowest $2^+$ states in $^{88}Sr$ and their relationship to corresponding single-particle excitations of $^{89}Y$. The neutron transition densities in this model result entirely from core polarization contributions to effective operators within the proton shell-model space. It is therefore of interest to determine the degree to which both the shape and magnitude of the neutron transition densities can be predicted for low-lying normal-parity excitations of $^{88}Sr$.

Consistent studies of electron and proton scattering can provide some of the most detailed experimental information for low-lying states. Precise transition charge densities can be measured with electron scattering [11, 12], whereas the radial form of neutron transition densities can be deduced from proton scattering provided that an accurate model of the reaction is available. We have fitted empirical effective interactions [13–19] for $135 \leq E_p \leq 650$ MeV using proton scattering data for self-conjugate targets, for which determination of the relevant transition densities by electron scattering min-

*Present address: Catholic University of America, Washington, DC 20064.
†Present address: Life College, Marietta, GA 30060.
‡Present address: Bowdoin College, Brunswick, ME 04011.

imizes uncertainties due to nuclear structure, and have shown that accurate transition densities can then be obtained for more general transitions [20–23].

Previous applications have considered valence-neutron nuclei for which multipole matrix elements are generally stronger for neutrons than for protons. In this paper, we apply these techniques to determine neutron transition densities for normal-parity states of the valence-proton nucleus $^{88}$Sr using new cross section and analyzing power data for the scattering of 200.4 MeV protons. Additional cross section data for 201.5 MeV protons due to Kouw *et al.* [24] are also included in the analysis. We have also obtained data for $^{88}$Sr$(p,p')$ at $E_p = 500$ MeV and have demonstrated that transition densities fitted to proton scattering data are almost independent of projectile energy [25]. Therefore, the accuracy of the fitted densities is commensurate with the uncertainties estimated by each of the independent analyses.

Shell-model calculations were performed in the open proton shell, including the $1f_{5/2}$, $2p_{3/2}$, $2p_{1/2}$, and $1g_{9/2}$ orbits. Single-particle energy levels were taken from data for $^{89}$Y. A semiempirical interaction based upon the $G$ matrix calculated for the Bonn potential by Nakayama *et al.* [26] was employed. The interaction was supplemented by empirical density-dependent corrections whose 10 parameters were fitted to 50 energy levels for $^{88}$Sr, $^{89}$Y, and $^{90}$Zr. Effective operators were computed in a Hartree-Fock approximation using a total of 1000 particle-hole, particle-particle, and hole-hole configurations spanning $10\hbar\omega$. Ground-state correlations up to 4p-4h (four-particle–four-hole) were evaluated using a self-consistency procedure which was iterated until the multipole strengths stabilized. Coupling between $(n\text{p},n\text{h})$ configurations plays a crucial role in describing the collectivity of low-lying normal-parity excitations. This approach is designated ORASM for operator renormalization approximation for the shell model; further details may be obtained from Ref. [27].

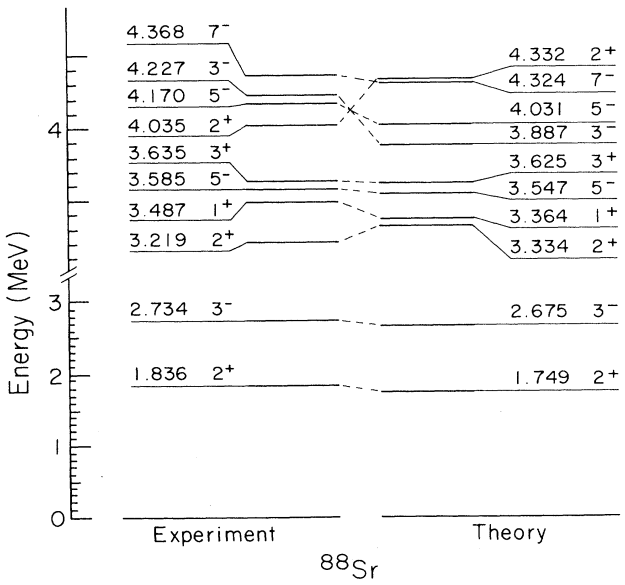


FIG. 1. Comparison between theoretical and experimental energies for selected states of $^{88}$Sr.

Selected experimental and theoretical energy levels for $^{88}$Sr are compared in Fig. 1. The agreement is quite close for the lowest $2^+$, $3^-$, $5^-$, and $7^-$ states, but begins to deteriorate for higher states of each multipolarity. The calculated energy is slightly too low for the $2_1^+$ state and a little too high for the $2_2^+$ state, but is rather too high for the $2_3^+$ state. Hence, we might expect the correspondence between physical and model $2^+$ states to become tenuous beyond the second $2^+$ state. Similarly, the agreement between theoretical and experimental energies for the second $3^-$ and $5^-$ states is also marginal.

The experiment is described in Sec. II. The data are compared with ORASM predictions in Sec. III. The procedures used to fit transition densities to the data are outlined in Sec. IV. Transition densities are fitted to the data and compared with the ORASM in Sec. V. Our conclusions are summarized in Sec. VI.

## II. EXPERIMENT

The experiment was performed at the Indiana University Cyclotron Facility (IUCF) using polarized protons with kinetic energy 200.4 MeV. The beam current was monitored with Faraday cups which measure the current in their left and right halves independently as a monitor of beam centering. For scattering angles $\theta \leq 27°$ a small Faraday cup was placed inside the scattering chamber. For angles $\theta \geq 27°$ a larger and more accurate Faraday cup outside the scattering chamber was used. The normalization of the internal cup relative to the external cup was determined to be 0.90. Maximum beam currents of 100 nA were used at backward angles, but currents less than 2 nA were used at forward angles to keep dead times below 10%.

The beam polarization was measured approximately every 8 h at a location between the injector and main-stage cyclotrons, where the energy was 15.21 MeV, using scattering from helium at $\pm 122°$, where the analyzing power is 0.992. Typical polarizations were 0.82 for spin up and 0.78 for spin down, with variations less than 0.03 between successive measurements.

Isotopically enriched metallic foils (> 99%) were used as targets. The thicknesses were measured at the beam position to $\pm 0.1$ mil accuracy using a micrometer. The areal thicknesses were $15.4 \pm 0.7$ and $28.8 \pm 0.7$ mg/cm$^2$. We estimate the systematic uncertainty in normalization to be about $\pm 5\%$.

Scattered protons were analyzed by the QDDM magnetic spectrometer, detected by a single helical wire chamber at the focal plane, and identified by a pair of $\Delta E/E$ scintillators. For each spectrometer setting, corrections to the nominal scattering angle were determined from the differential recoil between elastic scattering from $^{88}$Sr and from $^{12}$C and $^{16}$O impurities in the target. The solid angle was typically 18 mrad×20 mrad for large scattering angles, but was reduced to 10 mrad×10 mrad at the most forward angles.

A typical spectrum, with an energy resolution of about 80 keV FWHM, is shown in Fig. 2. The spectra were analyzed using the line-shape fitting code ALLFIT [28].

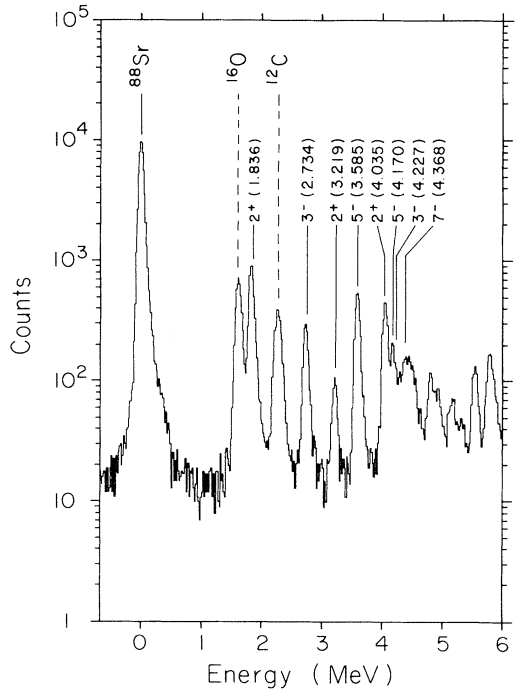


FIG. 2. Typical spectrum for $^{88}$Sr$(p,p')$ at $E_p = 200$ MeV. Peaks corresponding to the states of interest, and to impurities, are indicated. Note that the $3_2^-$ peak appears as a shoulder on the $5_2^-$ peak.

The separations between members of multiplets were constrained to known values so that reliable yields could be extracted for peaks separated by a little less than the experimental resolution. At the momentum transfer used in Fig. 2 the $3_2^-$ peak appears as a shoulder on a much stronger $5_2^-$ peak, whereas for smaller momentum transfer the $3_2^-$ peak tends to dominate near 4.2 MeV of excitation. Nevertheless, the smoothness of the extracted angular distributions demonstrates that, using appropriate constraints on the fitting procedure, the $5_2^-$ and $3_2^-$ peaks at 4.17 and 4.23 MeV could be reliably separated over most of the angular range. However, no fits were performed for higher excitation energies where the the spectrum becomes increasingly more complicated. For the $7_1^-$ state we rely on the data of Ref. [24], which had somewhat better resolution.

Measurements were made for angles between 8° and 44.5°, corresponding to momentum transfers between about 0.45 and 2.42 fm$^{-1}$. Complete data tables for 10 states are on deposit with the Physics Auxiliary Publication Service [29]. Additional cross section data from Orsay are available [24] for many of the states of interest and were included in the analysis.

## III. COMPARISON WITH ORASM CALCULATIONS

Calculations of proton scattering were made with the code LEA [30], which employs a zero-range approximation for exchange to reduce the nuclear structure requirements to a set of transition densities diagonal with respect to position [31]. We use the local density approximation based upon the density at the projectile position [32]. The 200 MeV empirical effective interaction [16], fitted to elastic and inelastic scattering from $^{16}$O and $^{40}$Ca simultaneously, was used for the isoscalar spin-independent central and spin-orbit components. Other components of the effective interaction were constructed from the Franey-Love $t$ matrix [33] by applying medium modifications deduced from the LR interaction of Ray [34]. The procedure is described in more detail in Ref. [17]. The density dependence for inelastic scattering is enhanced by the rearrangement factor derived by Cheon *et al.* [35]. Inelastic scattering was calculated in the distorted wave approximation using the optical potential calculated with the same effective interaction. The calculations and fits also include corrections for the finite spectrometer apertures used by the two experiments, but these effects are generally quite small.

Elastic scattering calculations are compared with the data in Fig. 3. The proton transition density was obtained by unfolding the nucleon form factor from the measured charge density. For simplicity, we assume that $\rho_n \propto \rho_p$. Excellent agreement with the data is then obtained for momentum transfers $q < 2$ fm$^{-1}$. The discrepancy between calculated and experimental analyzing powers for larger $q$ is probably due to small differences between the neutron and proton radial distributions because similar calculations for self-conjugate targets retain their accuracy for momentum transfers up to at least 2.7

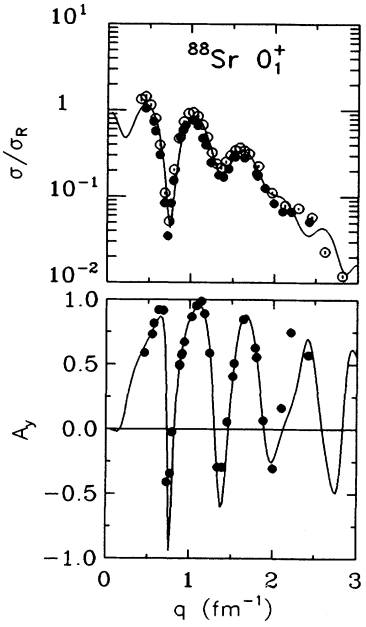


FIG. 3. Experimental differential cross section and analyzing power data for proton elastic scattering from $^{88}$Sr are compared with predictions (*solid lines*) based on an empirical effective interaction folded with measured $\tilde{\rho}_p(q)$ and the assumption that $\rho_n \propto \rho_p$. The solid circles are the data described here; the open circles are the data from Ref. [24]. To enhance detail, the elastic cross section is compared with the Rutherford cross section ($\sigma_R$) appropriate to the present form of the Schrödinger equation with relativistic kinematics.

fm$^{-1}$. Fortunately, inelastic scattering is not particularly sensitive to such large momentum components of the distorted waves. The apparent difference between the normalization of cross sections for the two data sets is discussed in Sec. IV C.

### A. 2$^+$ states

Calculations based upon the ORASM wave functions are compared with the data for 2$^+$ states in Fig. 4, in which the solid curves represent the full calculations and the short-dashed curves represent the contribution of the matter densities alone. For the $2_1^+$ state we also show as a long-dashed line the result of scaling the ORASM cross section prediction by a factor of $(1.29)^2 \approx 1.66$. The model evidently predicts the shape of the matter transition density for the $2_1^+$ state relatively well, but its amplitude must be enhanced by about 30%. We find also that the contribution of spin and current densities is negligible for the collective $2_1^+$ state.

The calculation for the $2_2^+$ state, on the other hand, is almost an order of magnitude below the first peak of the cross section and the model fails to describe the shape of either the cross section or the analyzing power angular distributions. Furthermore, of all the normal-parity excitations we have investigated for $^{88}$Sr, the spin and current densities make appreciable contributions only for the $2_2^+$ state. Similar effects were observed for the $2_2^+$ state of $^{34}$S [23], for which the shell model also fails to describe the angular distributions but predicts appreciable contributions for nonmatter densities. However, we found that those data are very well described by empirical matter densities alone, without need of important current or spin contributions. We show in Sec. IV A that the data for the $2_2^+$ state of $^{88}$Sr are also described very well by empirical matter densities alone. The analyzing power data for both of these cases exhibit oscillatory patterns characteristic of collective normal-parity excitations dominated by matter densities. Therefore, we expect the matter density to be responsible for the increase in the cross section and to overwhelm the contribution of nonmatter densities to the analyzing power. The primary effect of additional spin and current densities would be a small dilution of the analyzing power that results from the matter distribution alone.

Theoretical calculations for the third 2$^+$ model state differ markedly from the data for the third 2$^+$ state that is observed. Both the cross section and analyzing power angular distributions observed for this state are quite unusual in shape and, except for small momentum transfer, do not appear to be consistent with a 2$^+$ assignment. There is a nearby state that could not be resolved and which is tentatively identified as a 6$^-$ state [36], but the cross section computed from the theoretical wave function for the lowest 6$^-$ state is much too small to account for the uncharacteristic shape of the data for the peak at 4.03 MeV. We performed calculations for 4$^-$ states which appear in the model at similar energies, but we did not find an abnormal-parity candidate with sufficient strength to resolve this problem. The most likely explanation is that the third 2$^+$ state is predominantly a neutron excitation that lies outside the present shell-model space. The increasing discrepancy between theoretical and experimental energy levels for successive 2$^+$ states noted in the Introduction is consistent with this explanation.

### B. Negative-parity states

Theoretical calculations for the $3_1^-$, $5_1^-$, and $7_1^-$ states are compared with the data in Fig. 5 using a similar legend. The analyzing power data and the shape of the cross section angular distributions are described well for all three states, but to reproduce the cross section peaks the theoretical calculations must be adjusted by factors of approximately 1.15 for the $3_1^-$, 0.85 for the $5_1^-$, and 1.40 for the $7_1^-$ states.

Similar calculations for the $3_2^-$ and $5_2^-$ states, shown in Fig. 6, also describe the analyzing power data very well.

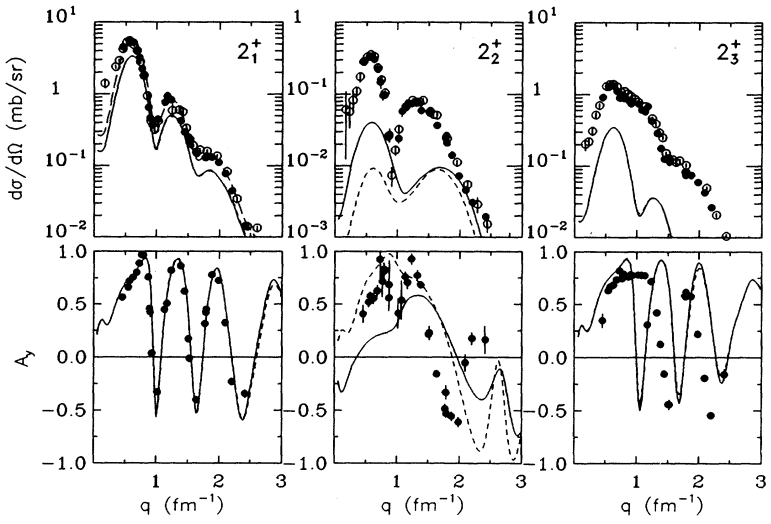


FIG. 4. Experimental differential cross section and analyzing power data for proton inelastic scattering to the lowest three 2$^+$ states in $^{88}$Sr are compared with predictions based on the ORASM densities with (*solid lines*) and without (*short dashes*) spin and current contributions. For the $2_1^+$ state, the *long dashes* represent $(1.29)^2$ times the ORASM cross section prediction. The solid circles are the data described here, the open circles are the data from Ref. [24]. Note that short-dashed and solid lines are often too close to discern.

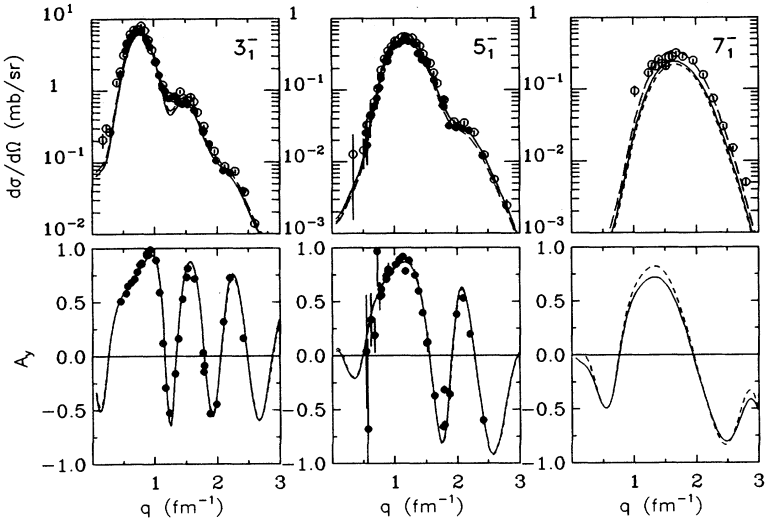


FIG. 5. Experimental differential cross section and analyzing power data for proton inelastic scattering to the lowest $3^-$, $5^-$, and $7^-$ states in $^{88}$Sr are compared with predictions based on the ORASM densities with (*solid lines*) and without (*short dashes*) spin and current contributions. The *long dashes* represent the ORASM cross section predictions multiplied by 1.15, 0.85, and 1.40 for the $3_1^-$, $5_1^-$, and $7_1^-$ states, respectively. The solid circles are the data described here; the open circles are the data from Ref. [24]. Note that short-dashed and solid lines are often too close to discern.

The cross section for the $3_2^-$ state does not require much adjustment of strength, but the discrepancies for moderate momentum transfers suggest that a modification of radial shape would be needed to fit the data. The cross section prediction for the $5_2^-$ state, on the other hand, needs little modification of shape but requires a rather large scale factor of about $(1.55)^2 \approx 2.4$ to reproduce the data.

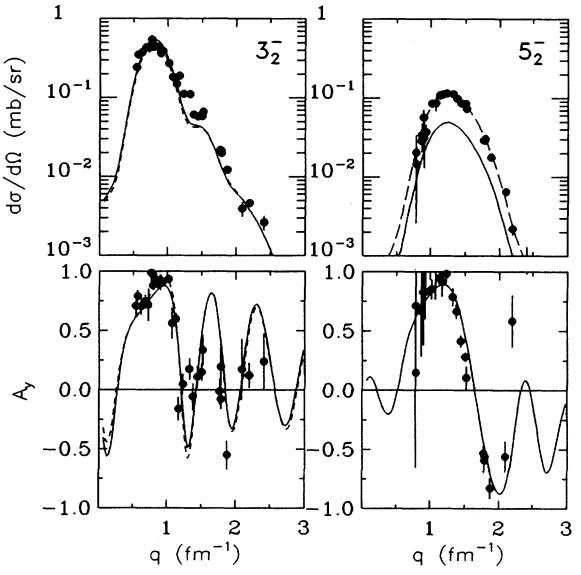


FIG. 6. Experimental differential cross section and analyzing power data for proton inelastic scattering to the $3_2^-$ and $5_2^-$ states in $^{88}$Sr are compared with predictions based on the ORASM densities with (*solid lines*) and without (*short dashes*) spin and current contributions. For the $5_2^-$ cross section, *long dashes* represent the ORASM calculation multiplied by 2.4. Note that short-dashed and solid lines are often too close to discern.

## IV. ANALYSIS PROCEDURES

### A. Transition densities

Transition charge densities $\rho_{\rm ch}(r)$ were fitted to electron scattering data by van der Bijl *et al.* [3]. These densities are represented by the Fourier-Bessel expansion (FBE)

$$\rho_{\rm ch}(r) = \sum_\nu a_\nu q_\nu j_L(q_\nu r) \tag{1}$$

within a cutoff radius $R = 11.0$ fm. The FBE frequencies are determined by the condition

$$j_{L-1}(q_\nu R) = 0.0. \tag{2}$$

Proton transition densities $\rho_p$ were then obtained by unfolding the nucleon form factor from the transition charge density $\rho_{\rm ch}$.

Neutron transition densities $\rho_n$ for a transition of multipolarity $L$ were parametrized using the Laguerre-Gaussian expansion (LGE)

$$\rho_n(r) = \sum_\nu a_\nu x^J e^{-x^2} L_\nu^\kappa(2x^2), \tag{3}$$

where $\kappa = L + \frac{1}{2}$ and $x = r/b$. The oscillator parameter $b = 2.2$ fm sets a convenient radial scale, but the analysis is essentially independent of $b$ because the LGE is complete. The densities were fitted to the proton scattering data using the methods described in Refs. [22, 23]. The analysis includes a high-$q$ bias and an estimate of the incompleteness error that results from limitation of the data to finite momentum transfer. A tail bias is used to damp unphysical oscillations of the density for $r \geq r_m$, where we assume that $\rho \propto e^{-dr}$ beyond the match radius $r_m = 6.5$ fm. We chose $d = 3.0$ fm$^{-1}$ based upon examination of the theoretical densities and of the quantity $r^{L+2}\,\rho(r)$ that is used as the integrand in computing the transition amplitude; this quantity is discussed more

thoroughly in the next section.

We assume that spin and current densities can be neglected for the relatively strong normal-parity transitions considered herein. We have tested the sensitivity of the $2_2^+$ results to possible spin and current contributions by including theoretical estimates of these densities as fixed input. We find that the fitted densities are not affected by the presence of spin and current contributions at the present level of sensitivity. The only visible effect of these additional contributions is a slight damping of the analyzing power calculation for small momentum transfer. Although this effect does improve the agreement with the data, the failure of the theoretical wave function to describe the cross section casts doubt upon the reliability of the nonmatter densities also. Therefore, the final analysis for this state is limited to matter densities alone.

Additional fits to the data near the first peak of the angular distributions for each state were made using the simpler scaling hypothesis $\rho_n = S\rho_p$, where $S$ is an adjustable scaling parameter. Comparison between LGE and scaling fits provides a useful guide to the sensitivity of the analysis to differences between the shapes of the neutron and proton transition densities.

### B. Moments and ratios

The transition strength is customarily defined by a moment

$$M = \int dr\, r^{L+2} \rho_L(r) \tag{4}$$

which strongly emphasizes the density for large radii through the weighting factor $r^{L+2}$. It is difficult to extract model-independent values for proton and neutron matrix elements, $M_p$ and $M_n$, from electron and proton scattering data unless unusually precise data are available for very low momentum transfer. Otherwise, it is necessary to apply a tail bias to the fitted density for large radii and to carefully constrain the integrand $r^{L+2}\rho_L$. Unfortunately, many analyses, including the analysis of $^{88}$Sr$(e,e')$ by van der Bijl [3], fail to properly constrain the tail and permit unphysical oscillations to persist at very large radii. Even when considerable care is given to the tail bias, imperfections in the data in localized regions of momentum transfer tend to promote unlikely structures in fitted densities at large radii. The $M_n$ and $M_p$ values can then depend upon the details of the tail bias, such as the choice of match radius or slope, too strongly.

Scattering experiments for intermediate momentum transfers, typically $0.25 \leq q \leq 3.0$ fm$^{-1}$, provide accurate measurements of transition densities for intermediate radii, typically $1 \lesssim r \lesssim 8$ fm, but determine neither very long nor very short wavelengths. The analysis of such data using general expansions of the radial density requires regularization through both high momentum transfer and large radius constraints. Thus, long-wavelength quantities such as $M_n$ and $M_p$ cannot be determined in a truly model-independent fashion.

A more reliable measure of the relative contributions of neutrons and protons to a transition may be found in the ratio

$$R_{np} = \tilde{\rho}_n(q_n)/\tilde{\rho}_p(q_p), \tag{5}$$

where

$$\tilde{\rho}_\lambda(q) = \int dr\, r^2 j_L(qr)\rho_\lambda(r) \tag{6}$$

is the Fourier transform of the proton or neutron transition density for ($\lambda = p$ or $n$) and where $q_\lambda$ corresponds to the momentum transfer for which $\tilde{\rho}_\lambda$ attains its maximum value. Since $q_\lambda$ is usually well within the experimental range of momentum transfer, the $\tilde{\rho}_\lambda(q_\lambda)$ values are determined with relatively small uncertainty and very little model dependence. In our tests, variations of the tail bias which produce as much as 20% variations in $M_n$, with virtually no effect upon the fit to the data, result in less than 1% variations of $\tilde{\rho}_n(q_n)$. Furthermore, we find that when the densities are sufficiently similar in shape for scaling fits, based upon the assumption $\rho_n = S\rho_p$, to successfully describe data for momentum transfers below the second diffraction peak, then the fitted values of $R_{np}$ and $S$ usually agree to within their uncertainties. Therefore, $R_{np}$ represents a nearly model-independent measure of transition strength that is more relevant to inelastic scattering experiments than moments which depend upon extremely large radii and small momentum transfer.

### C. Normalization

Examination of the figures shown in Sec. III reveals a systematic normalization difference between the IUCF and Orsay cross section measurements of 10–15 %. The target employed in the Orsay experiment used a paraffin coating to reduce oxidation, but the coating could not be removed for a thickness measurement and the data did not extend to small enough angles for normalization via the Coulomb cross section. Hence, an independent measurement was performed with 22 MeV protons and the thickness was determined by comparison with an optical model calculation for small angles. The uncertainty in the target thickness obtained by this procedure was estimated to be ±10%, including model dependence [24].

Although the calculated elastic cross section shown in Fig. 3 falls between the two data sets, the theory is not yet sufficiently accurate for elastic scattering by heavy targets to use as a normalization standard. We observe that application of a factor of about 0.8 to the Orsay data brings the two data sets into good agreement. However, the renormalization required to reconcile the inelastic cross sections is closer to 0.9. This factor was determined from scale factor fits to the data for the $2_1^+$, $2_2^+$, $3_1^-$, and $5_1^-$ states. Since we are most interested in the inelastic data, we have applied the factor of 0.9 to the Orsay data so that both data sets could be included in the analysis.

The uncertainty in the fitted neutron density due to uncertainties in normalization was determined from the variation of the fitted density due to independent renormalization of the two data sets. The total normalization

uncertainty was obtained by adding the separate contributions in quadrature. We assumed that the normalization uncertainties are ±5% for the present experiment and ±10% for the Orsay experiment. Unlike the charge density, for which an adjustment of the $(e,e')$ normalization results in a direct scaling of the fitted density, the uncertainty in the neutron density depends upon normalization more strongly than linearly because the contribution of $\rho_p$ to $(p,p')$ is held fixed throughout the analysis so that normalization adjustments must be made entirely by changes in the fitted neutron density.

We performed fits to the two data sets independently and find little qualitative difference between the resulting neutron transition densities even without renormalization of the Orsay data. Although the differences are somewhat larger for states with smaller values of $R_{np}$, these differences never affect the conclusions drawn below. Moreover, excellent agreement is obtained using the renormalization factor quoted above.

## V. TRANSITION DENSITY RESULTS

The fits to the data are displayed in Figs. 7–9, where the solid curves represent the LGE analysis and the dashed curves represent the scaling analysis. The LGE coefficients for $\rho_n$ are tabulated in Table I. The moments $M_n$ and $M_p$, the scale factors $S$, and the $R_{np}$ ratios are compared with theoretical predictions in Table II. The

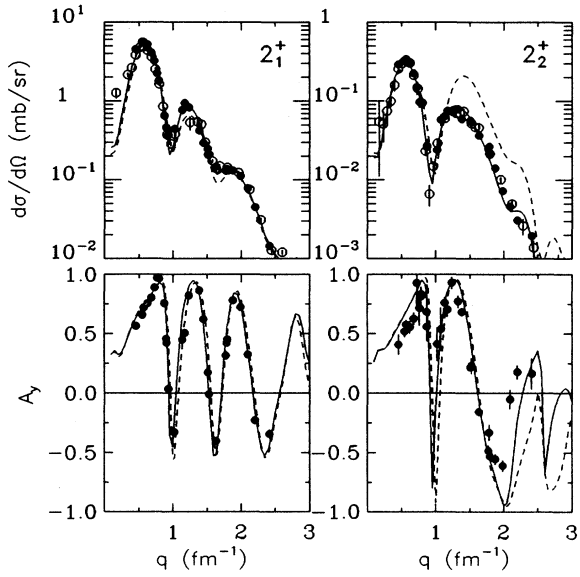


FIG. 7. Experimental differential cross section and analyzing power data for proton inelastic scattering to the lowest two $2^+$ states in $^{88}$Sr are compared with the results of fitting the parameters of our model to the data (*solid lines*) and to the results of scaling the neutron density as $\rho_n = S\rho_p$ (*dashed lines*). The solid circles are the data described here; the open circles are the data from Ref. [24] scaled by a factor of 0.9.

TABLE I. Neutron transition density parameters for $^{88}$Sr. $a_n$ are the LGE coefficients as in Eq. (3) and are expressed in units of fm$^{-3}$; these coefficients are based upon $b = 2.20$ fm.

| $n$ | $2_1^+$ | $2_2^+$ | $3_1^-$ | $3_2^-$ |
|---|---|---|---|---|
| 1 | (-3.41±8.71)×10$^{-4}$ | (-7.33±0.58)×10$^{-3}$ | ( 1.95±0.12)×10$^{-2}$ | (-4.37±0.56)×10$^{-3}$ |
| 2 | (-1.14±0.07)×10$^{-2}$ | (-8.49±0.43)×10$^{-3}$ | (-1.39±0.07)×10$^{-2}$ | ( 7.18±0.29)×10$^{-3}$ |
| 3 | ( 1.22±0.06)×10$^{-2}$ | ( 1.92±0.12)×10$^{-3}$ | ( 5.16±0.31)×10$^{-3}$ | (-1.00±0.08)×10$^{-3}$ |
| 4 | (-1.65±0.19)×10$^{-3}$ | (-6.83±0.74)×10$^{-4}$ | ( 1.20±1.38)×10$^{-4}$ | (-2.46±0.29)×10$^{-4}$ |
| 5 | (-4.46±1.23)×10$^{-4}$ | ( 1.44±0.33)×10$^{-4}$ | (-2.02±0.88)×10$^{-4}$ | ( 8.43±1.58)×10$^{-5}$ |
| 6 | ( 6.88±5.83)×10$^{-5}$ | ( 5.62±1.87)×10$^{-5}$ | (-3.53±4.52)×10$^{-5}$ | ( 2.14±0.70)×10$^{-5}$ |
| 7 | ( 1.40±4.09)×10$^{-5}$ | (-3.40±1.16)×10$^{-5}$ | (-0.65±2.95)×10$^{-5}$ | (-9.32±5.09)×10$^{-6}$ |
| 8 | (-0.19±2.45)×10$^{-5}$ | (-8.01±5.84)×10$^{-6}$ | (-0.20±1.98)×10$^{-5}$ | (-4.13±2.40)×10$^{-6}$ |
| 9 | ( 0.11±1.56)×10$^{-5}$ | ( 7.30±4.26)×10$^{-6}$ | ( 0.00±1.05)×10$^{-5}$ | ( 0.35±1.33)×10$^{-6}$ |
| 10 | ( 0.60±6.64)×10$^{-6}$ | ( 4.54±1.93)×10$^{-6}$ | ( 0.15±3.70)×10$^{-6}$ | ( 6.28±6.06)×10$^{-7}$ |
| 11 | ( 0.04±1.61)×10$^{-6}$ | ( 1.10±0.48)×10$^{-6}$ | ( 0.27±7.89)×10$^{-7}$ | ( 1.84±1.52)×10$^{-7}$ |
| 12 | (-0.13±1.78)×10$^{-7}$ | ( 1.09±0.55)×10$^{-7}$ | ( 0.00±8.04)×10$^{-8}$ | ( 2.08±1.72)×10$^{-8}$ |

| $n$ | $5_1^-$ | $5_2^-$ | $7_1^-$ |
|---|---|---|---|
| 1 | ( 5.11±0.23)×10$^{-3}$ | ( 2.96±0.37)×10$^{-3}$ | ( 1.65±0.23)×10$^{-3}$ |
| 2 | (-1.10±0.09)×10$^{-3}$ | (-1.56±0.74)×10$^{-4}$ | (-4.84±1.76)×10$^{-5}$ |
| 3 | ( 2.43±1.85)×10$^{-5}$ | ( 9.68±2.31)×10$^{-5}$ | ( 0.16±9.25)×10$^{-6}$ |
| 4 | ( 2.95±0.74)×10$^{-5}$ | ( 2.98±1.14)×10$^{-5}$ | ( 1.56±2.82)×10$^{-6}$ |
| 5 | (-1.11±2.98)×10$^{-6}$ | ( 2.19±5.67)×10$^{-6}$ | (-1.64±1.44)×10$^{-6}$ |
| 6 | (-1.44±1.72)×10$^{-6}$ | (-0.29±2.82)×10$^{-6}$ | (-6.17±6.72)×10$^{-7}$ |
| 7 | (-0.45±7.65)×10$^{-7}$ | (-0.02±1.67)×10$^{-6}$ | ( 1.66±3.41)×10$^{-7}$ |
| 8 | ( 0.56±4.88)×10$^{-7}$ | ( 0.08±9.23)×10$^{-7}$ | ( 2.09±1.90)×10$^{-7}$ |
| 9 | ( 0.02±2.63)×10$^{-7}$ | (-0.01±3.79)×10$^{-7}$ | ( 8.85±7.92)×10$^{-8}$ |
| 10 | (-0.37±9.23)×10$^{-8}$ | ( 0.00±1.08)×10$^{-7}$ | ( 2.25±2.29)×10$^{-8}$ |
| 11 | (-0.07±1.98)×10$^{-8}$ | ( 0.01±1.96)×10$^{-8}$ | ( 3.50±4.28)×10$^{-9}$ |
| 12 | (-0.02±2.07)×10$^{-9}$ | ( 0.03±1.79)×10$^{-9}$ | ( 2.70±4.09)×10$^{-10}$ |

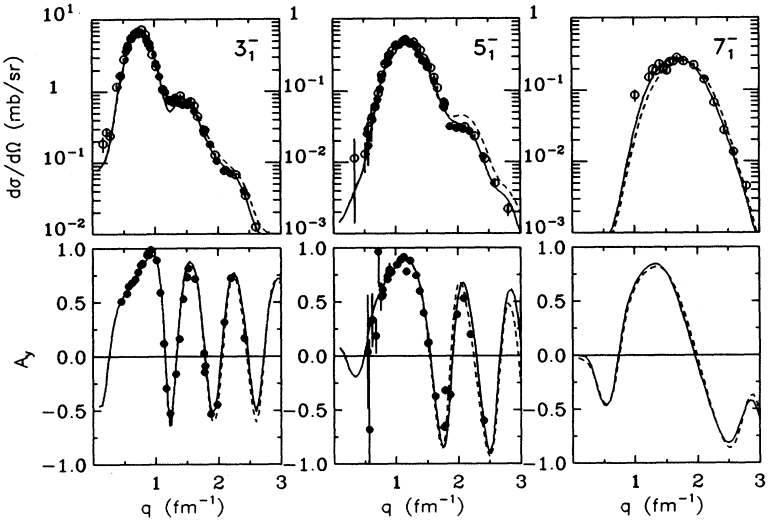


FIG. 8. Experimental differential cross section and analyzing power data for proton inelastic scattering to the lowest $3^-$, $5^-$, and $7^-$ states in $^{88}$Sr are compared with the results of fitting the parameters of our model to the data (*solid lines*) and to the results of scaling the neutron density as $\rho_n = S\rho_p$ (*dashed lines*). The solid circles are the data described here; the open circles are the data from Ref. [24] scaled by a factor of 0.9.

uncertainties quoted for $M_n/M_p$ and $R_{np}$ do not include uncertainties in $\rho_p$ because the proton transition densities were assumed to be known from electron scattering and were not varied during the fitting procedures for $\rho_n$. For most states we find that the scale factor fits describe the data almost as well as the more sophisticated LGE fits, demonstrating that the neutron and proton transition densities for most states have similar shapes. For the $2_2^+$ state, on the other hand, the scale factor analysis produces a second maximum far stronger than exhibited by the data, demonstrating that the data for this state are quite sensitive to the detailed shape of the neutron transition density. The data for this state, and all the others, are described very well by the LGE analysis.

Despite the significant differences between the shapes of the neutron and proton transitions densities for several states, the fitted values of $R_{np}$ always agree very well with the fitted scale factors. The agreement between those quantities is much closer than the agreement with the $M_n/M_p$ ratios. This observation supports the identification of $R_{np}$ as the functional of density that most closely resembles the result of traditional scaling analyses.

The experimental charge and neutron densities are

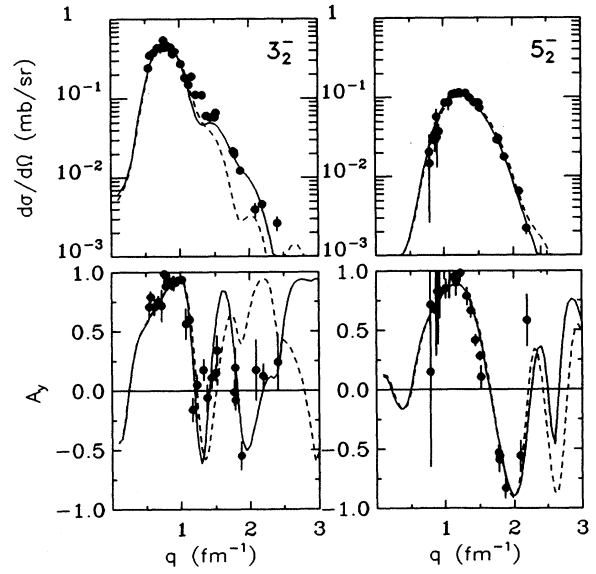


FIG. 9. Experimental differential cross section and analyzing power data for proton inelastic scattering to the second lowest $3^-$ and $5^-$ states in $^{88}$Sr are compared with the results of fitting the parameters of our model to the data (*solid lines*) and to the results of scaling the neutron density as $\rho_n = S\rho_p$ (*dashed lines*).

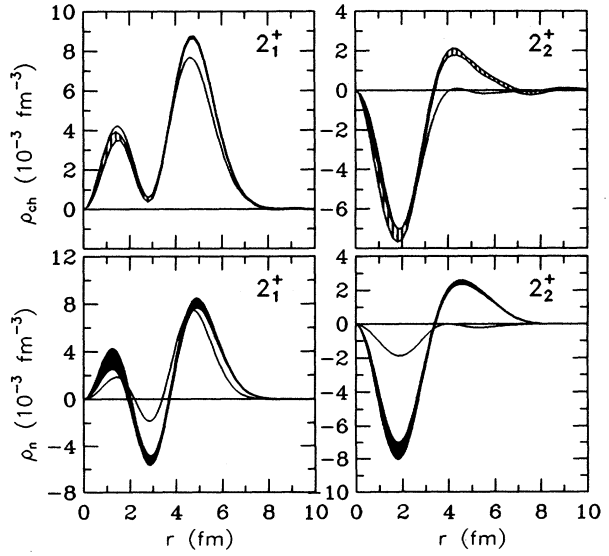


FIG. 10. Radial distributions of the experimental charge and neutron transition densities (*bands*) for inelastic scattering to the lowest two $2^+$ states in $^{88}$Sr are compared with predictions based on the ORASM (*solid lines*).

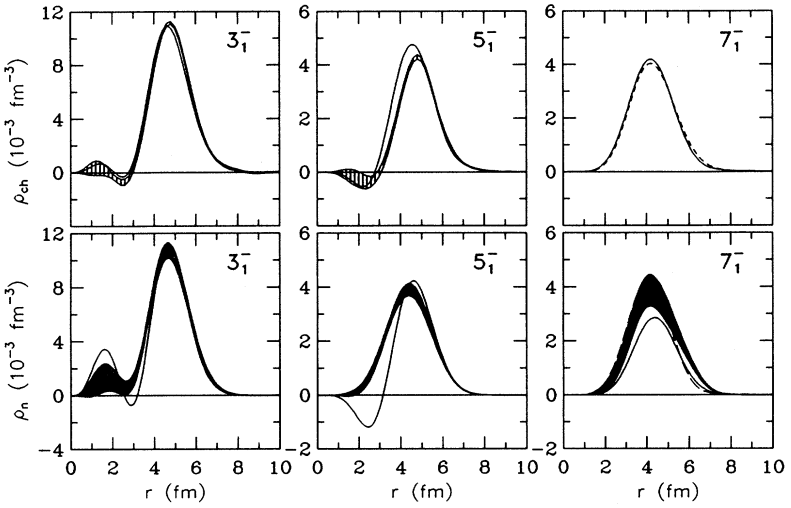


FIG. 11. Radial distributions of the experimental charge and neutron transitions densities (*bands*) for inelastic scattering to the $3_1^-$, $5_1^-$, and $7_1^-$ states in $^{88}$Sr are compared with ORASM predictions. For the $3_1^-$ and $5_1^-$ densities and for the $7_1^-$ neutron density, the ORASM calculations are shown as solid lines, but for the $7_1^-$ charge density we use a short-dashed line because a band is not available for the experimental density. The scaled density, $\rho_n = S\rho_p$, is shown for the $7^-$ state as a long-dashed line.

compared with the ORASM predictions in Figs. 10–12. The error bands for the charge densities include both statistical and incompleteness errors. The charge density for the $7^-$ state does not carry an error band because the $(e, e')$ data for that state were analyzed using a single-particle transition rather than a FBE density. The error bands for the neutron densities also include uncertainties due to normalization of the cross sections for the two data sets independently. The incompleteness error tends to dominate the error bands for small radii, whereas statistical and normalization errors dominate for larger radii. The error band for the $7^-$ state is relatively wide due to the uncertainty in the normalization of the Orsay data.

### A. The $2^+$ states

The shell-model wave functions for the lowest two $2^+$ states are fairly well approximated by two orthogonal linear combinations of $\pi(2p_{1/2}, 1f_{5/2}^{-1})$ and $\pi(2p_{1/2}, 2p_{3/2}^{-1})$, where for the charge density these two configurations interfere constructively for the lowest state and destructively for the next. This model has been shown to give a relatively good description of earlier electron scattering data by Schwentker *et al.* [1, 4]. The neutron transition densities in the present model result entirely from core polarization contributions to the effective operators constructed for use in the proton model space. It is therefore of interest to determine the degree to which both the shape and magnitude of the neutron transition densities can be predicted without explicit participation of neutrons in the shell-model space.

The experimental $2_1^+$ densities for both protons and neutrons are similar in shape to the theoretical densities, but are somewhat stronger at the surface. This surface enhancement increases both $M_n$ and $M_p$ with respect to theoretical estimates, but the ratio $M_n/M_p$ is similar for both theory and experiment. This state is apparently more collective than predicted by the model, but the isospin structure is similar. The most likely possibility is that the $(g_{9/2})^2$ effective charge is underestimated by the model. Increasing the isoscalar contribution from this configuration would enhance the surface densities and increase the $M_n/M_p$ ratio.

The model reproduces the experimental $2_2^+$ charge density for $r < 3$ fm, but fails to predict the surface lobe for larger radii. This feature can be described, at least qualitatively, with modest changes of the shell-model amplitudes for the two dominant configurations. Similarly, the neutron density predicted by the model is similar in shape to the proton density, but is smaller in amplitude, and again fails to reproduce the surface lobe required to fit the $(p, p')$ data. Due to absorption, which increases the relative contribution of surface lobes with respect to

TABLE II. Comparison of the experimentally extracted moments, scale factors, and $R_{np}$ with theoretical predictions. Uncertainties in the final digit are given in parentheses. Uncertainities in $M_p^{\rm expt}$ are omitted because $\rho_p$ was held fixed in the fitting procedure. The units of $M_n$ and $M_p$ are fm$^L$ for multipolarity $L$.

| State | $S$ | $R_{np}^{\rm expt}$ | $R_{np}^{\rm th}$ | $M_n^{\rm expt}$ | $M_p^{\rm expt}$ | $M_n^{\rm expt}/M_p^{\rm expt}$ | $M_n^{\rm th}$ | $M_p^{\rm th}$ | $M_n^{\rm th}/M_p^{\rm th}$ |
|---|---|---|---|---|---|---|---|---|---|
| $2_1^+$ | 0.81(4) | 0.81(4) | 0.80 | 12.6(4) | 13.3 | 0.95(3) | 9.22 | 12.01 | 0.77 |
| $2_2^+$ | 2.20(8) | 2.14(8) | 0.25 | 4.10(15) | 1.92 | 2.14(8) | -0.52 | -0.83 | 0.63 |
| $3_1^-$ | 0.87(4) | 0.88(4) | 0.87 | 89.0(35) | 96.1 | 0.93(4) | 79.8 | 92.6 | 0.86 |
| $3_2^-$ | 1.26(5) | 1.20(4) | 0.79 | 26.7(10) | 20.4 | 1.31(5) | 21.5 | 26.2 | 0.82 |
| $5_1^-$ | 0.71(4) | 0.76(7) | 0.72 | 872(55) | 1297 | 0.67(4) | 926 | 1358. | 0.68 |
| $5_2^-$ | 0.63(4) | 0.63(5) | 0.64 | 372(43) | 552 | 0.67(8) | 224 | 304 | 0.74 |
| $7_1^-$ | 0.70(10) | 0.76(10) | 0.56 | $3.2(5)\times10^4$ | $3.53\times10^4$ | 0.91(14) | $1.93\times10^4$ | $3.52\times10^4$ | 0.55 |

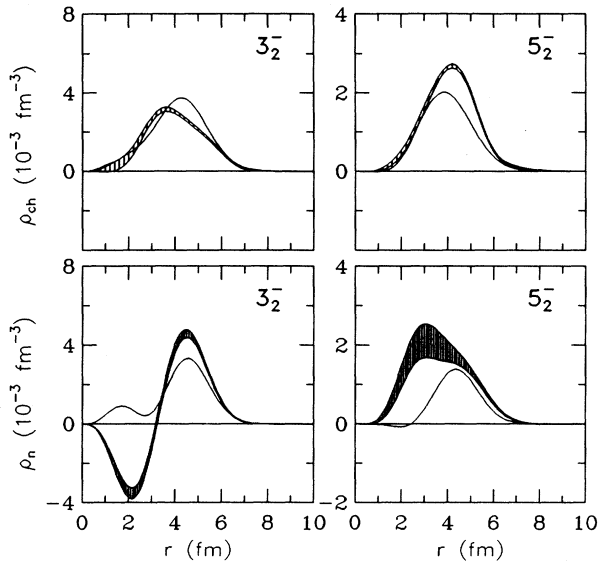


FIG. 12. Radial distributions of the experimental charge and neutron transitions densities (*bands*) for inelastic scattering to the $3_2^-$ and $5_2^-$ states in $^{88}$Sr are compared with prediction based on the ORASM (*solid lines*).

interior lobes, these surface lobes are critical to proton scattering. Without the surface lobes the cross sections calculated from the theoretical densities are about an order of magnitude below the data for small momentum transfers. The interior lobes are then needed to fit the data for larger momentum transfers at and beyond the second maximum. From these data we determine that the interior lobe of the neutron transition density is much stronger than predicted by the theory and is, in fact, even stronger than the corresponding lobe of the proton density. The ratio $R_{np} = 2.14(8)$ is much stronger than the theoretical prediction 0.25. The theoretical values of $M_n/M_p$ and $R_{np}$ are quite different for the $2_2^+$ state because the shapes for $\tilde{\rho}_n(q)$ and $\tilde{\rho}_p(q)$ are also quite different.

Similar conclusions for the $2_2^+$ state were reached by Kouw *et al.* [24] using calculations based upon wave functions from the one broken pair model (1BP) of Hengeveld *et al.* [8]. The 1BP model reproduces the essential features of the charge density and does predict a significant surface lobe, but the ratio between the surface and interior lobes is still smaller than observed. Similarly, the 1BP neutron density is strongest in the interior, but is weaker than the proton density. To describe the qualitative features of their $(p,p')$ cross section data, Kouw *et al.* [24] constructed transition densities from linear combinations of the 1BP densities for the $2_1^+$ and $2_2^+$ states. The resulting $\rho_n$ and $\rho_p$ for the $2_2^+$ state both have prominent surface lobes and they find that the low-$q$ cross section is dominated by the neutron contribution, which contradicts theoretical expectations but is consistent with our findings. However, their model fails to achieve adequate high-$q$ strength because the interior lobe of the $\rho_n$ density is too small. Of course, the densities fitted using the more general LGE model reproduce the entire angular distribution.

For single-closed-shell nuclei, the experimental $M_n/M_p$ ratio for the lowest $2^+$ state is typically greater than $N/Z$ if the neutron shell is open or less than $N/Z$ if the proton shell is open. For the second $2^+$ state, ratios on the opposite side of $N/Z$ are usually found, such that $M_n/M_p < N/Z$ for open neutron shells or $M_n/M_p > N/Z$ for open proton shells [37, 38]. This observation has been called the *reversal effect* by Brown, Bernstein, and Madsen [39] and was attributed to pairing correlations which deplete the nominally closed shell and contribute $0\hbar\omega$ configurations that are otherwise absent.

The data for $^{88}$Sr are consistent with the reversal effect, but the ORASM calculation is not. The ORASM predicts that all low-lying normal-parity excitations should have $M_n/M_p < 1$, but the data for the $2_2^+$ state give a ratio that is considerably larger than both unity and $N/Z$. The model also fails to reproduce the surface lobes observed for both proton and neutron densities. The surface lobe for neutrons probably arises from $\nu(2d_{5/2}^2, 1g_{9/2}^{-2})$ configurations and for protons from $\pi(1g_{9/2}^2, 2p_{3/2}^{-2})$ configurations, both of which could be related to enhancement of the $g_{9/2}$ effective charge.

### B. Negative-parity states

The data for the lowest $3^-$, $5^-$, and $7^-$ states are described very well by the simple assumption of proportionality between neutron and proton transition densities. The ORASM calculations describe the shapes of the $3_1^-$ charge and neutron densities remarkably well, even in the interior. The experimental $5_1^-$ densities both appear to be shifted outwards relative to the model, but both neutron and proton densities have very similar shapes and the ratio of their strengths is consistent with theoretical expectations. The model successfully predicts the quenching of the $E7$ single-particle strength observed in the $7_1^-$ charge density, which is almost identical with the model prediction, but the neutron density is considerably stronger than predicted and is shifted outward slightly. The model predicts $R_{np} = 0.56$ for the $7_1^-$ state, whereas a ratio of $R_{np} = 0.76(10)$ is observed. Perhaps the effective interaction coupling the core to the valence space falls too rapidly with momentum transfer to reproduce the transition amplitude for larger $L$ values.

The data for the $3_2^-$ and $5_2^-$ states are of marginal quality for the LGE analysis. Nevertheless, despite the large differences between the shapes of the neutron and proton densities for each state, the fitted values of $S$ and $R_{np}$ agree very well. The LGE model increases the high-$q$ cross section for the $3_2^-$ state using a strong interior lobe in $\rho_n$. This lobe is considerably stronger and opposite in sign compared with the theoretical prediction. An experiment with better resolution would be useful to confirm this interesting result. However, we also note that the charge densities for both states are also somewhat unusual. The experimental charge density for the $3_2^-$ state appears to be depleted in the surface region where the

theoretical density peaks, whereas for the $5_2^-$ state it is enhanced at larger radius and exhibits an unusually steep slope. Possible errors in such features could distort the fitted neutron densities. Uncertainties of this type are not included in the error bands and would be most significant for states which are difficult to resolve in either experiment.

### C. Interior sensitivity

The sensitivity of proton scattering to the interior neutron density was studied extensively in Ref. [40] using a pseudodata technique. It was shown that the neutron density used to produce the pseudodata could be recovered with a relatively narrow error band that represents the intrinsic sensitivity of the reaction. However, that method does not account for systematic errors due to limitations of the reaction model. For heavy nuclei the differences between cross sections computed for various models of the neutron density are often so small that even though the correct densities can be recovered from pseudodata there is concern that the systematic errors may be too large for reliable application of this method to real data for heavy nuclei. One way to address this concern is to analyze data for two or more projectile energies that are far enough apart that the systematic errors in the reaction model should be uncorrelated. We have applied this method to the analysis of $^{48}$Ca$(p,p')$ at 200, 318, and 500 MeV and find that the error bands produced by our analysis procedures do in fact represent realistic estimates of the uncertainties in fitted neutron densities [41]. This method is applied in Ref. [25] to the more difficult case of $^{88}$Sr, by comparing analyses for 200 and 500 MeV, and we again find that quite similar results are obtained for both energies.

Alternatively, the sensitivity of proton scattering data to the interior density can be examined using *notch* calculations in which the scattering potential for $r \leq R_N$ is set to zero. The dependence of $\chi^2$ upon $R_N$ is then an indication of interior sensitivity. Note that we apply the notch to the scattering potential instead of to the density itself in order to avoid ringing when performing convolutions in momentum space. Thus, the onset of interior sensitivity actually occurs for radii somewhat smaller than $R_N$ due to the range of the interaction.

The scattering potentials were calculated using the fitted densities from Table I. For simplicity we omit the aperture corrections and compare with the present data only. Note that somewhat better values of $\chi^2$ would have been obtained using densities fitted to these data alone, but the qualitative behavior of $\chi^2(R_N)$ is independent of these considerations.

Results for selected normal-parity transitions are shown in Fig. 13. For the states with surface-peaked densities, such as the $2_1^+$, $3_1^-$, and $5_1^-$ states, appreciable sensitivity appears to develop for $r > 3$ fm. For the $2_2^+$ state, for which the transition density has more interior structure, sensitivity develops as early as $r > 1$ fm. Since the density is required to approach the origin as $r^L$ and high-frequency structures are limited by the high-$q$

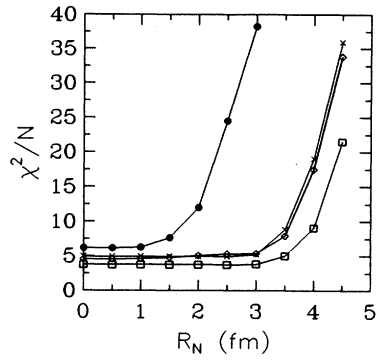


FIG. 13. The *goodness of fit* ($\chi^2$ *per datum*) vs notch radius ($R_N$) is used as a measure of the sensitivity of proton scattering to the interior of the nucleus. The transition densities are held constant, but the scattering potentials inside $R_N$ are set to zero. Due to the range of the interaction, sensitivity to the interior density occurs for radii somewhat smaller than $R_N$. Results for the $2_2^+$ state are shown as solid points, for the $2_1^+$ state as diamonds, for the $3_1^-$ state as crosses, and for the $5_1^-$ state as squares.

bias, these physical constraints allow little freedom for smaller radii so that the error band remains finite even for small $r$. In addition, the range of the interaction also confers some sensitivity to radii smaller than the knee in the $\chi^2(R_N)$ curves for each state. These considerations explain the relatively narrow interior bands for the surface-peaked densities and the tight bands for densities of interior character. Although the interior bands are wider for higher energies due to increased absorption, appreciable interior sensitivity remains for the $2_2^+$ state. In that case absorption reduces the cross section, but if the transition is observed with a distinctive angular distribution, the probe must have been sufficiently penetrating to reach the interior lobe.

It is also instructive to examine the dependence of calculated cross sections and analyzing powers upon the notch radius. Figure 14 shows calculations for several values of $R_N$ for both the $2_1^+$ and $2_2^+$ states of $^{88}$Sr. For the $2_1^+$ state it appears that the sensitivity to $r \leq 3$ fm is relatively small and perhaps similar to the uncertainties in the reaction mechanism. However, data at higher momentum transfer could enhance the interior sensitivity, provided that both the effective interaction and the proton density are known with sufficient accuracy. For the $2_2^+$ state, on the other hand, densities inside of 2 fm can surely be measured with confidence. Therefore, the difference between the $2_1^+$ and $2_2^+$ angular distributions is clearly due to the contrast between surface-peaked and interior densities. These results demonstrate that proton inelastic scattering is capable of measuring interior transition densities for states with prominent interior lobes.

Also note that as $R_N$ increases the calculated angular distributions for both states become similar in shape because the notch limits the probe to the surface, $r > R_N$,

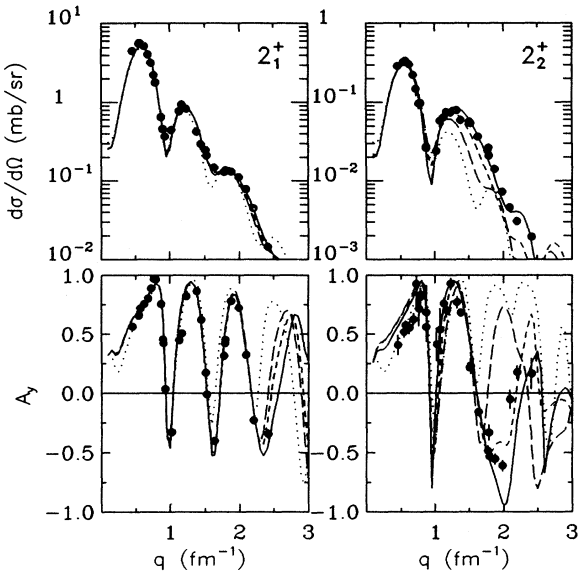


FIG. 14. Cross section and analyzing power calculations for various notch radii $R_N$ illustrate the sensitivity of these quantities to the interior of the nucleus. The solid circles are the data described here for the lowest two $2^+$ states of $^{88}$Sr. Calculations for $R_N$ =0, 2, 3, and 4 fm are shown as solid lines, short dashes, long dashes, and dots, respectively.

where only the strength but not the shape is significant. Thus, use of large $R_N$ corresponds to strong absorption and gives results comparable to those for strongly absorbed reactions, such as alpha scattering.

## VI. SUMMARY AND CONCLUSIONS

We have obtained new cross section and analyzing power data for the scattering of 200 MeV protons from $^{88}$Sr and have analyzed these data, in conjunction with some earlier cross section data, using an empirical effective interaction calibrated upon proton scattering data for both $^{16}$O and $^{40}$Ca. We had previously established that the empirical effective interaction is sufficiently accurate for use in the extraction of neutron transition densities from proton scattering data for normal-parity excitations. Neutron transition densities were fitted to the present data for two $2^+$, two $3^-$, two $5^-$, and one $7^-$ states. The results were compared with a shell-model calculation using an empirical density-dependent interaction and a Hartree-Fock approximation to construct effective operators and transition densities.

We find relatively good agreement between theory and experiment for the $2_1^+$, $3_1^-$, and $5_1^-$ states, but neutron densities for the $2_2^+$ and $7_1^-$ states are considerably stronger than predicted. The transition densities for the $2_2^+$ state have strong interior lobes, as expected from the theory, but also have significant surface lobes that are absent from the theoretical densities. The interior lobe of the $2_2^+$ proton density is well described by the model, but the interior lobe of the experimental neutron density is unexpectedly strong. The surface lobes enhance the cross section for low momentum transfer by about an order of magnitude over theoretical predictions based upon densities without the surface features. The data clearly determine the full radial form of the neutron transition density for this state with good sensitivity.

We have proposed a robust measure of the relative neutron and proton transition strengths, $R_{np}$, based upon the peak form factors that is more suitable to the analysis of inelastic scattering experiments than $M_n/M_p$ because it employs measured rather than extrapolated quantities and consequently is less sensitive to ambiguities in the behavior of transition densities at large radii. Although the proton and neutron densities are similar in shape for most states, there are some notable differences. For example, although the data for the $3_2^-$ state are marginal for the LGE analysis, the fitted neutron density appears to possess an interior lobe that is absent from the proton density and which is much stronger and opposite in sign than the theoretical prediction. Nevertheless, scaling and LGE analyses of the ratio between neutron and proton transition amplitudes, $R_{np}$, are consistent for all transitions that were analyzed despite these shape differences.

The best available shell-model interactions are based upon realistic nucleon-nucleon interactions supplemented by phenomenological parameters adjusted to reproduce selected nuclear data. These data are usually limited to energy levels and transition strengths. Now that both neutron and proton transition densities can be measured with good accuracy, perhaps the optimization procedures can be extended to consider radial information also. The availability of complete transition densities should facilitate a more critical examination of effective operators constructed for use with shell-model calculations within practical model spaces.

This work was supported in part by the National Science Foundation (Grant No. PHY-8615512).

[1] O. Schwentker, J. Dawson, S. McCaffrey, J. Robb, J. Heisenberg, J. Lichtenstadt, C. N. Papanicolas, J. Wise, J. S. McCarthy, N. Hintz, and H. P. Blok, Phys. Lett. **112B**, 40 (1982).

[2] E. J. Kaptein, Ph.D. thesis, Vrije Universiteit, Amsterdam, 1978.

[3] L. T. van der Bijl, Ph.D. thesis, Vrije Universiteit, Amsterdam, 1982.

[4] O. Schwentker, J. Dawson, J. Rob, J. Heisenberg, J. Lichtenstadt, C. N. Papanicolas, J. Wise, J. S. McCarthy, L. T. van der Bijl, and H. P. Blok, Phys. Rev. Lett. **50**, 15 (1983).

[5] J. Heisenberg, J. Dawson, T. Milliman, O. Schwentker, J. Lichtenstadt, C. N. Papanicolas, J. Wise, J. S. McCarthy, N. Hintz, and H. P. Blok, Phys. Rev. C **29**, 97 (1984).

[6] T. E. Milliman, J. H. Heisenberg, F. W. Hersman, J. P. Connelly, C. N. Papanicolas, J. E. Wise, H. P. Blok, and L. T. van der Bijl, Phys. Rev. C **32**, 805 (1985).

[7] M. Morlet, C. Djalali, N. Marty, A. Willis, J. C. Jourdain, L. R. Kouw, and H. P. Blok, Nucl. Phys. **A439**, 253 (1985).
[8] W. Hengeveld, K. Allaart, and W. H. Dickoff, Nucl. Phys. **A435**, 381 (1985).
[9] T. E. Milliman, J. P. Connelly, J. H. Heisenberg, F. W. Hersman, J. E. Wise, and C. N. Papanicolas, Phys. Rev. C **41**, 2586 (1990).
[10] B. S. Flanders, J. J. Kelly, K. K. Seth, B. Parker, M. Artuso, R. Soundranayagm, F. W. Hersman, and J. P. Connelly, Bull. Am. Phys. Soc. **32**, 1121 (1987); F. W. Hersman, J. R. Calarco, J. Heisenberg, T. Milliman, J. J. Kelly, A. Scott, F. T. Baker, V. Penumetcha, A. Bacher, G. T. Emery, C. Olmer, W. Jones, and M. Grimm, *ibid.* **29**, 628 (1984).
[11] J. Heisenberg, Adv. Nucl. Phys. **12**, 61 (1981).
[12] J. Heisenberg and H. P. Blok, Annu. Rev. Nucl. Part. Sci. **33**, 569 (1983).
[13] J. J. Kelly, Phys. Rev. C **39**, 2120 (1989).
[14] J. J. Kelly, J. M. Finn, W. Bertozzi, T. N. Buti, F. W. Hersman, C. Hyde-Wright, M. V. Hynes, M. A. Kovash, B. Murdock, P. Ulmer, A. D. Bacher, G. T. Emery, C. C. Foster, W. P. Jones, D. W. Miller, and B. L. Berman, Phys. Rev. C **41**, 2504 (1990).
[15] Q. Chen, J. J. Kelly, P. P. Singh, M. C. Radhakrishna, W. P. Jones, and H. Nann, Phys. Rev. C **41**, 2514 (1990).
[16] H. Seifert, J. J. Kelly, A. E. Feldman, B. S. Flanders, M. A. Khandaker, Q. Chen, P. Karen, B. E. Norum, P. Welch, and A. Scott (submitted to Phys. Rev. C).
[17] J. J. Kelly, A. E. Feldman, B. S. Flanders, H. Seifert, D. Lopiano, B. Aas, A. Azizi, G. Igo, G. Weston, C. Whitten, A. Wong, M. V. Hynes, J. McClelland, W. Bertozzi, J. M. Finn, C. E. Hyde-Wright, R. W. Lourie, P. E. Ulmer, B. E. Norum, and B. L. Berman, Phys. Rev. C **43**, 1272 (1991).
[18] J. J. Kelly, P. Boberg, A. E. Feldman, B. S. Flanders, M. A. Khandaker, S. D. Hyman, H. Seifert, P. Karen, B. E. Norum, P. Welch, S. Nanda, and A. Saha, Phys. Rev. C **44**, 2602 (1991).
[19] B. S. Flanders, J. J. Kelly, H. Seifert, D. Lopiano, B. Aas, A. Azizi, G. Igo, G. Weston, C. Whitten, A. Wong, M. V. Hynes, J. McClelland, W. Bertozzi, J. M. Finn, C. E. Hyde-Wright, R. W. Lourie, B. E. Norum, P. Ulmer, and B. L. Berman, Phys. Rev. C **43**, 2103 (1991).
[20] J. J. Kelly, W. Bertozzi, T. N. Buti, J. M. Finn, F. W. Hersman, M. V. Hynes, C. Hyde-Wright, B. E. Norum, A. D. Bacher, G. T. Emery, C. C. Foster, W. P. Jones, D. W. Miller, B. L. Berman, J. A. Carr, and F. Petrovich, Phys. Lett. **169B**, 157 (1986).
[21] J. J. Kelly, Q. Chen, P. P. Singh, M. C. Radhakrishna, and W. P. Jones, Phys. Rev. C **41**, 2525 (1990).
[22] J. J. Kelly, M. A. Khandaker, P. Boberg, A. E. Feldman, B. S. Flanders, S. Hyman, H. Seifert, P. Karen, B. E. Norum, P. Welch, S. Nanda, and A. Saha, Phys. Rev. C **44**, 1963 (1991).
[23] M. A. Khandaker, J. J. Kelly, P. Boberg, A. E. Feldman, B. S. Flanders, S. Hyman, H. Seifert, P. Karen, B. E. Norum, P. Welch, S. Nanda, and A. Saha, Phys. Rev. C **44**, 1978 (1991).
[24] L. R. Kouw, H. P. Blok, and J. Blok, Nucl. Phys. **A481**, 13 (1988).
[25] B. S. Flanders, J. J. Kelly, F. W. Hersman, J. H. Heisenberg, J. P. Connelly, K. K. Seth, B. Parker, M. Artuso, and R. Soundranayagm (unpublished).
[26] K. Nakayama, S. Krewald, J. Speth, and W. G. Love, Phys. Nucl. Phys. **A431**, 419 (1984).
[27] J. H. Heisenberg (unpublished).
[28] J. J. Kelly, computer program ALLFIT (unpublished).
[29] See AIP document No. PAPS PRVCA-47-1615-10 for 10 pages containing a complete tabulation of the data described in this paper. Order by PAPS number and journal reference from American Institute of Physics, Physics Auxiliary Publication Service, 500 Sunnyside Boulevard, Woodbury, New York 11797-2999. The price is $1.50 for each microfiche (60 pages) or $5.00 for photocopies of up to 30 pages, and $0.15 for each additional page over 30 pages. Air mail additional. Make checks payable to the American Institute of Physics.
[30] J. J. Kelly, computer program LEA (unpublished).
[31] F. Petrovich, R. J. Philpott, A. W. Carpenter, and J. A. Carr, Nucl. Phys. **A425**, 609 (1984).
[32] J. J. Kelly, W. Bertozzi, T. N. Buti, J. M. Finn, F. W. Hersman, C. E. Hyde-Wright, M. V. Hynes, M. A. Kovash, B. Murdock, B. E. Norum, B. Pugh, F. N. Rad, A. D. Bacher, G. T. Emery, C. C. Foster, W. P. Jones, D. W. Miller, B. L. Berman, W. G. Love, J. A. Carr, and F. Petrovich, Phys. Rev. C **39**, 1222 (1989).
[33] M. A. Franey and W. G. Love, Phys. Rev. C **31**, 488 (1985).
[34] L. Ray, Phys. Rev. C **41**, 2816 (1990).
[35] T. Cheon, K. Takayanagi, and K. Yazaki, Nucl. Phys. **A437**, 301 (1985); **A445**, 227 (1985); T. Cheon and K. Yazaki, *ibid.* **A455**, 653 (1986).
[36] C. M. Lederer and V. S. Shirley, *Table of Isotopes* (Wiley, New York, 1978).
[37] A. M. Bernstein, V. R. Brown, and V. A. Madsen, Phys. Rev. Lett. **42**, 425 (1979).
[38] A. M. Bernstein, V. R. Brown, and V. A. Madsen, Phys. Lett. **103B**, 255 (1981).
[39] V. R. Brown, A. M. Bernstein, and V. A. Madsen, Phys. Lett. **164B**, 217 (1985).
[40] J. J. Kelly, Phys. Rev. C **37**, 520 (1988); J. A. Carr, F. Petrovich, and J. Kelly, in *Neutron-Nucleus Collisions—A Probe of Nuclear Structure* (Burr Oak State Park, Glouster, Ohio), Proceedings of the Conference on Neutron-Nucleus Collisions—A Probe of Nuclear Structure, AIP Conf. Proc. No. 124, edited by J. Rapaport, R. W. Finlay, S. M. Grimes, and F. Dietrich (AIP, New York, 1984), p. 230.
[41] A. E. Feldman, P. Boberg, B. S. Flanders, S. D. Hyman, J. J. Kelly, M. A. Khandaker, H. Seifert, P. Karen, B. E. Norum, P. Welch, A. Saha, S. Nanda, Q. Chen, and A. Scott, Bull. Am. Phys. Soc. **35**, 1038 (1990); A. E. Feldman, Ph.D. thesis, University of Maryland, 1991.